

Sea-Ice Melt Driven by Ice-Ocean Stresses on the Mesoscale

 Mukund Gupta¹ , John Marshall¹, Hajoon Song² , Jean-Michel Campin¹ , and Gianluca Meneghello¹ 
¹Department of Earth, Atmosphere and Planetary Sciences, Massachusetts Institute of Technology, Cambridge, MA, USA, ²Department of Atmospheric Sciences, Yonsei University, Seoul, South Korea

Key Points:

- Sea-ice drag on mesoscale ocean eddies can generate Ekman pumping and bring warm waters up to the surface
- In a process model, this reduces the ice thickness by 10% and the mixed layer depth by up to 60% in winter and spring
- Sea-ice formation (melt) in cyclones (anticyclones) produce deeper (shallower) mixed layer depths

Correspondence to:

 M. Gupta,
guptam@mit.edu
Citation:

 Gupta, M., Marshall, J., Song, H., Campin, J.-M., & Meneghello, G. (2020). Sea-ice melt driven by ice-ocean stresses on the mesoscale. *Journal of Geophysical Research: Oceans*, 125, e2020JC016404. <https://doi.org/10.1029/2020JC016404>

 Received 17 MAY 2020
 Accepted 21 OCT 2020

Abstract The seasonal ice zone around both the Arctic and the Antarctic coasts is typically characterized by warm and salty waters underlying a cold and fresh layer that insulates sea-ice floating at the surface from vertical heat fluxes. Here, we explore how a mesoscale eddy field rubbing against ice at the surface can, through Ekman-induced vertical motion, bring warm waters up to the surface and partially melt the ice. We dub this the “Eddy-Ice-Pumping” (EIP) mechanism. When sea-ice is relatively motionless, underlying mesoscale eddies experience a surface drag that generates Ekman upwelling in anticyclones and downwelling in cyclones. An eddy composite analysis of a Southern Ocean eddy channel model, capturing the interaction of the mesoscale with sea-ice, shows that within the compact ice zone, the mixed layer depth (MLD) is shallow in anticyclones (~20 m) due to sea-ice melt and deep in cyclones (~50–200m) due to brine rejection. “EIP” warms the core of anticyclones without significantly affecting the temperature of cyclones, producing a net upward vertical heat flux that reduces the mean sea-ice thickness by 10% and shoals the MLD by 60% over the course of winter and spring. In the following months, the sea-ice thickness recovers with an overshoot, due to strong negative feedbacks associated with atmospheric cooling and salt stratification. Consequently, the effect of “EIP” does not accumulate over the years, but modulates the seasonal cycle of ice within the compact ice zone.

Plain Language Summary Polar oceans typically have cold, fresh waters at the surface and warmer, saltier waters below that. When the atmospheric temperature is cold enough, the top layer of the ocean cools to the freezing point and sea-ice forms at the surface. This growth can be impeded by warmer waters at the subsurface, whose heat can melt sea-ice at its base. The effectiveness of this melting depends on the amount of heat transported from the deeper layers of the ocean up to the surface underneath the ice. This study explores a novel mechanism by which frictional interactions between ocean and sea-ice can increase the amount of heat delivered to the surface. At small scales (30–100 km), when the ocean rubs against relatively stationary sea-ice, it experiences a torque that drives vertical motions in the water column. This process brings warmer waters in contact with sea-ice and can reduce its mean thickness by 10% over the course of winter and spring. In the following months, the ice thickness recovers due to restoring processes, such that this mechanism does not lead to accumulated melt over the years, but changes the seasonality of sea-ice.

1. Introduction

The sea-ice zone surrounding both the Arctic and Antarctic coasts is vulnerable to melt from underlying warm waters residing at depth. In the Southern Ocean, upper circumpolar deep waters (UCDWs) flow below the surface near the continental shelf, where their heat influences both marine-terminating glaciers and sea-ice (Ackley et al., 2015; McKee et al., 2019; Orsi et al., 1995). The Antarctic upper ocean is relatively weakly stratified, such that heat stored at depth may readily be ventilated to the surface. In winter, typical ocean heat fluxes to sea-ice may reach 25–35 W m⁻² (Martinson & Iannuzzi, 1989). Ackley et al. (2015) measure heat fluxes of about 8 W m⁻² under pack ice in the Bellingshausen Sea and 17 W m⁻² under fast ice in the Amundsen Sea, consistent with co-located sea-ice melt rates. In the Arctic, the upper ocean is more strongly stratified, such that the direct influence of deep water-masses on sea-ice melt tends to be weaker. Intermediate Pacific Waters often flow in between the surface layer and warm Atlantic waters, shielding sea-ice from their heat (Carmack et al., 2015). The Arctic is also more quiescent, resulting in relatively weak vertical heat exchanges within the ocean interior (Lenn et al., 2009). Nevertheless, remnant summer waters

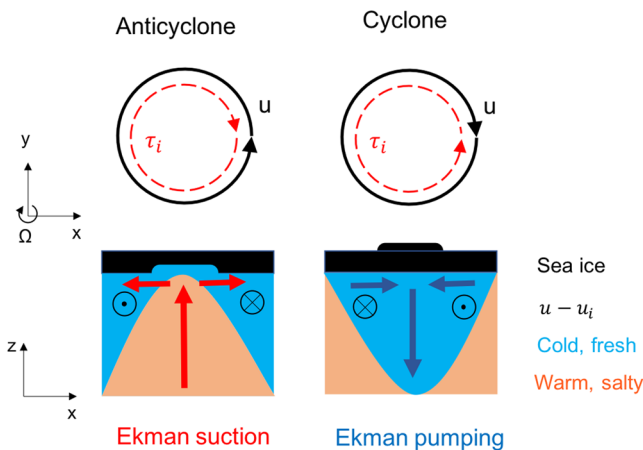


Figure 1. Schematic of the “Eddy-Ice-Pumping” mechanism in the Southern hemisphere. When sea-ice is stationary relative to the eddy, the ice-ocean stress τ_i opposes the eddy motion u , driving Ekman suction in anticyclones and Ekman pumping in cyclones. Upwelling of warm waters may melt sea-ice in anticyclones, whereas downwelling in cyclones may shield sea-ice away from warm waters, potentially allowing for thicker ice growth.

trapped below the surface mixed layer may effectively deliver basal heat to the ice and slow its growth in the winter (Jackson et al., 2012). Bathymetric constraints can also help deliver Atlantic waters directly to the surface (Onarheim et al., 2014), causing peak heat flux values of about 20 W m^{-2} under ice in certain regions (McPhee et al., 2003). With rising oceanic temperatures, the role of these vertical heat fluxes on sea-ice melt is likely to keep increasing, as it has in the Arctic over the last decades (Polyakov et al., 2017). Future changes in sea-ice coverage and seasonality may also have a global impact through their influence on deep and bottom water formation in the Arctic (Mauritzen & Häkkinen, 1997) and Antarctic (Ohshima et al., 2016), respectively.

The coarse resolution of Global Climate Models limits their ability to faithfully reproduce some of the fine scale physical processes responsible for vertical heat fluxes underneath sea-ice. These mechanisms may include double-diffusive mixing (Padman, 1995; Sirevaag & Fer, 2012; Timmermans et al., 2008), mesoscale eddy stirring (McKee et al., 2019), convection driven by brine rejection (Martinson & Iannuzzi, 1989) or interactions with the bathymetry (Muench et al., 2001), turbulence generated by ice/ocean drag (Ackley et al., 2015), inertial/tidal oscillations (Geiger et al., 1998), and internal wave mixing (Timmermans & Marshall, 2020). Over the Western Antarctic peninsula, McKee et al. (2019) present evidence that mesoscale eddies are responsible for delivering UCDWs to the continental shelf, consistent with the observa-

tions of Moffat and Meredith (2018). In the Arctic marginal ice zone (MIZ), previous studies have highlighted the importance of ocean eddies in the processes of heat and mass exchanges that control the sea-ice distribution (Johannessen et al., 1987; Niebauer & Smith, 1989). Manucharyan and Thompson (2017) describe a process by which intense, but small-scale, horizontal density gradients in the MIZ can enhance vertical velocities at the submesoscale and upwell warm waters to the surface.

This study explores a related mechanism termed “Eddy-Ice-Pumping” (EIP), by which frictional ice/ocean interactions at the mesoscale may intensify vertical velocities within eddies and drive upward heat fluxes underneath the ice. In regions where the ice concentration is large enough to resist motion driven by eddies, sea-ice exerts a net drag τ_i upon the ocean surface, which opposes the eddy velocity u . As illustrated in Figure 1, this mechanism generates surface divergence and Ekman upwelling in anticyclones, while driving surface convergence and Ekman downwelling in cyclones. Given the temperature inversion underneath the ice, one expects an advection of warm waters toward the ice in anticyclones and away from the ice in cyclones. We investigate how this mechanism affects the vertical structure of eddies and the overall melting rates in regions of compact sea-ice.

The modulation of eddy vertical velocities by surface stresses has been discussed in the context of air-sea interactions in the open ocean (Gaube et al., 2015; McGillicuddy et al., 2007; Song et al., 2020). The difference between surface winds and currents can drive both a monopole (Dewar & Flierl, 1987) and a dipole (Niiler, 1969; Stern, 1965) response in vertical velocities within eddies. Gaube et al. (2015) also find that Ekman velocities induced by sea surface temperature (SST) gradients can be significant in western boundary currents and in the Antarctic Circumpolar Current. Depending on their persistence, these vertical motions can significantly influence the life-cycle, structure, and transport properties of eddies (McGillicuddy, 2016). In the context of ice-ocean interactions, the problem has been studied by Hunkins (1981), Manley and Hunkins (1985), and Ou and Gordon (1986). Here, we examine the effectiveness of EIP at generating an eddy-scale curl in surface stress, and discuss whether the induced vertical velocities are persistent and large enough to affect the local profiles of temperature and salinity. We are also interested in how EIP couples with melting and freezing processes occurring in the seasonal ice zone.

The study is structured as follows: Section 2 describes the Southern Ocean eddying channel model used to investigate the EIP mechanism. Section 3 explores the conditions under which this process occurs in the

model. Section 4 presents an eddy composite analysis that highlights differences between the open ocean and the compact ice zone, the asymmetric response of cyclones and anticyclones to EIP, and the resulting modulation of sea-ice melt and formation. Section 5 describes the aggregate effects of EIP over a seasonal cycle and over multiple years in the compact ice zone. Section 6 discusses the main findings of this study and concludes.

2. The 3D Channel Model

Numerical experiments are conducted using an eddy ocean-ice channel model based on the MIT general circulation model (MITgcm; Adcroft et al., 1997; Marshall et al., 1997a, 1997b) representing the Southern Ocean and its seasonal ice zone. The domain has dimensions of 1,200 km by 3,200 km in the zonal and meridional directions respectively, with 4.08 km horizontal resolution. The east and west boundaries are connected, such that when fluid leaves from one side, it re-enters from the other. There are 50 vertical levels from the surface to the flat ocean bottom at 4,000 m. The vertical resolution ranges from 10 m in the top 50 m up to 100 m near the bottom. At the Southern boundary, there is a 300 m deep and 80 km wide shelf, followed by a 220 km wide continental slope that drops to the bottom. This setup was introduced in Doddridge et al. (2019).

The model is initialized using temperature and salinity profiles from the World Ocean Atlas version 2 (Locarnini et al., 2013; Zweng et al., 2013) along 30°E and repeated in the zonal direction. The northern boundary has a 100 km wide sponge layer over which temperature and salinity are relaxed to the initial conditions on a 10-day timescale. At the surface, the channel is forced through bulk formulae (Large & Pond, 1982) by monthly mean atmospheric fields from the Corrected Normal Year Forcing Version 2.0 taken along 30°E (Large & Yeager, 2009). The surface input data comprises shortwave and longwave radiation, air temperature, humidity, precipitation, snow fall, and wind speeds at 10 m height. As with the initial conditions, the atmospheric fields are extended across the channel, such that there is no zonal variation in surface forcing. Vertical mixing is based on the turbulent kinetic energy scheme by Gaspar et al. (1990), without convective adjustment. The model implements a nonlinear equation of state that uses a horizontally and temporally constant pressure according to Jackett and McDougall (1995).

The sea-ice model is based on the formulation detailed in Losch et al. (2010). It uses a continuum representation of sea-ice properties such as concentration, thickness, and velocity. Sea-ice thermodynamics employs the three-layer model of Winton (2000), where ice and snow thicknesses are calculated using heat fluxes from the top and bottom surfaces. Sea-ice dynamics are based on the elastic-viscous-plastic formulation by Hunke and Dukowicz (1997) in which atmospheric, oceanic, and internal stresses drive the sea-ice motion. The ice/ocean stress $\bar{\tau}_i$ is parameterized as follows:

$$\bar{\tau}_i = \rho_0 C_d (\bar{u} - \bar{u}_i) |\bar{u} - \bar{u}_i|, \quad (1)$$

where ρ_0 is the ocean density, C_d is a drag coefficient, \bar{u} is the horizontal surface ocean velocity, and \bar{u}_i is the sea-ice velocity. The turning angle is assumed to be zero and the drag coefficient is kept to a constant value of $C_d = 5.17 \times 10^{-3}$, consistent with the work of Mazloff et al. (2010) in the context of the Southern Ocean State Estimate. The ice/ocean heat flux is parameterized as:

$$F_b = c_w \rho_s \gamma u^* (T_s - T_f), \quad (2)$$

where c_w and ρ_s are the ocean's specific heat capacity and surface density, respectively, γ is a nondimensional heat transfer coefficient, T_s is the surface temperature below ice, T_f is the ocean freezing point, and u^* is a friction velocity between ice and ocean. The parameter γ is fixed to 0.006 and the friction velocity is estimated as $u^* = \sqrt{0.0054 v_s^2}$, where v_s is the surface ocean velocity.

At the start of the simulation, the sea-ice thickness is initialized to 1 m, covering the entire model domain south of 56°S. The model is integrated for 50 years, by which time it reaches a quasi-equilibrium. In

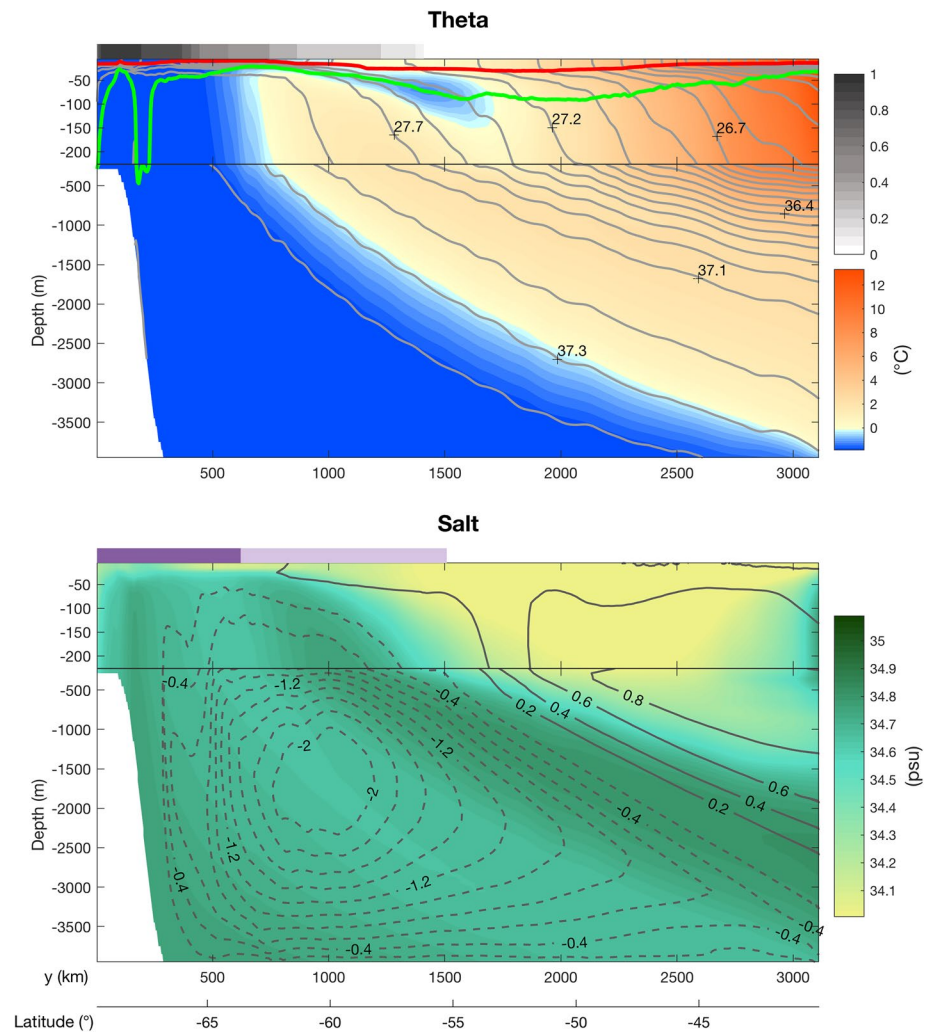


Figure 2. Annual and zonal mean state of the channel model at quasi-equilibrium. (Top) Potential temperature (filled contours), potential density σ_0 (gray line contours in the top 210 m), and σ_2 (gray contours between 210 and 4,000 m). The annual mean sea-ice fraction is shown in the gray bars at the top of the panel. The colored lines show the summer (red) and winter (green) mixed layer depth. (Bottom) Salt (filled contours) and residual stream function in Sv [$= 10^6 \cdot \text{m}^3 \text{s}^{-1}$] (gray line contours, filled clockwise, and dashed anticlockwise). The solid bars at the top of the panel indicate the minimum (dark purple) and maximum (light purple) sea-ice extent. The temperature color bar diverges at 0°C to highlight differences between cold water-masses. South of $y = 500$ km, the mean temperature is between -1.7°C and -1.8°C at all depths.

Figure 2, the potential temperature distribution highlights a temperature inversion between $y = 400$ – $1,600$ km, where cold and fresh waters in the top 10–100 m of the water column lie above warm and salty waters of northern origin. The residual meridional circulation consists of two overturning cells that upwell to surface around $y = 800$ km, bringing relatively warm waters in close proximity to the seasonal ice zone. In the top 50–100 m underneath the ice, isopycnals are relatively flat, due to the salinity stratification. We define the mixed layer depth (MLD) as the depth at which the local difference in potential density with respect to the overlying surface value is: $\Delta\sigma_0 = 0.02 \text{ kg m}^{-3}$, which is a midrange threshold consistent with past work (Holte & Talley, 2009; Toole et al., 2010; Wilson et al., 2019). Our conclusions are generally not sensitive to this choice, although the magnitude of MLD variations may change with the particular threshold selected. The climatological MLD ranges between 10 and 80 m in the summer over the whole domain, but can deepen significantly in winter between $y = 0$ – 600 km due to bottom water formation.

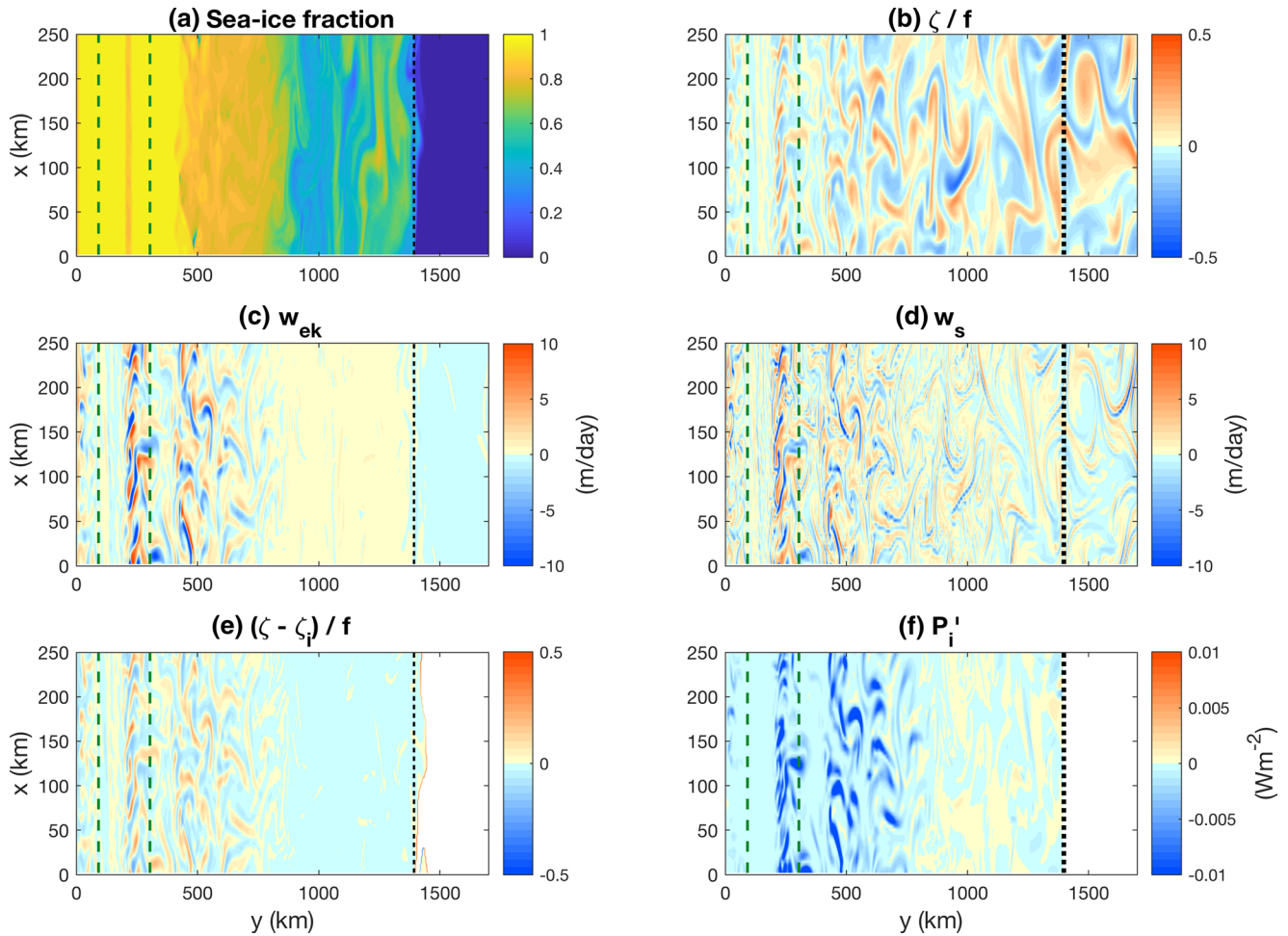


Figure 3. Snapshots taken in September and shown over a subset of the model domain for (a) sea-ice fraction, (b) normalized surface vorticity ζ/f , (c) Ekman vertical velocity w_{ek} , (d) subsurface vertical velocity w_s , (e) normalized surface vorticity minus sea-ice vorticity $(\zeta - \zeta_i)/f$, and (f) eddy power transfer between ice and ocean P_i' . The green dashed lines show the limits of the continental slope and the shelf, and the dotted black line shows the zonal mean sea-ice edge.

3. Exploration of “EIP” in an Idealized Model

Figure 3 shows EIP at play from a snapshot of the channel model's ice zone taken in September. During that month, sea-ice cover is at its maximum extent, and a region of compact sea-ice develops in the southern part of the channel (panel a). The Rossby number (ζ/f , in panel b) reaches peak values of 0.5, and there is evidence of both cyclonic and anticyclonic mesoscale eddies present under the ice. The horizontal length-scale of these eddies ranges from tens to hundreds of kilometers and increases from south to north, due to the influences of the beta effect and the continental slope on the first baroclinic Rossby radius of deformation ($R_d = NH/f$). Using representative values of $N = 10^{-3} \text{ s}^{-1}$, $f = 10^{-4} \text{ s}^{-1}$ and $H = 250\text{--}4,000 \text{ m}$ gives an R_d of 40 km off the shelf and 2.5 km on the shelf. The model's horizontal spacing of 4.08 km can therefore resolve mesoscale eddy features in the open ocean, but can neither resolve nor permit them over the shelf. The band-like structure seen between $y = 0\text{--}400 \text{ km}$ in ζ/f and other quantities in Figure 3 is the result of using a wind forcing that is uniform in the zonal direction.

Panel (c) shows the vertical Ekman velocity w_{ek} computed as:

$$w_{ek} = \frac{1}{\rho_0} \nabla \times \left(\frac{\bar{\tau}}{f} \right), \quad (3)$$

where the net ocean stress $\bar{\tau}$ is a linear combination of the ice-ocean stress $\bar{\tau}_i$ and the wind-ocean stress $\bar{\tau}_w$, weighted by the sea-ice fraction α as follows:

$$\bar{\tau} = \alpha \bar{\tau}_i + (1 - \alpha) \bar{\tau}_w. \quad (4)$$

Between $y = 0$ –800 km, where the sea-ice fraction is high ($\geq 80\%$), there is a small-scale pattern of w_{ek} with magnitudes reaching up to 10 m day^{-1} . In this region, the pattern in w_{ek} is reflected on the subsurface vertical velocity w_s diagnosed at the first vertical model layer (5 m depth) and shown in panel (d). In regions of loose ice ($y = 800$ –1,400 km), the difference between the sea-ice and ocean vorticities (ζ and ζ_i , shown in panel e) is negligibly small, reflecting a regime where sea-ice drift is strongly influenced by underlying ocean currents. On the other hand, when ice is compact, ζ and ζ_i are largely decoupled, due to internal stresses restricting the ice motion. The transfer of energy between ocean and sea-ice P_i can be computed as follows:

$$P_i = \bar{\tau}_i \cdot \bar{u}, \quad (5)$$

Panel (f) shows the eddying component of P_i , defined as:

$$P_i' = \bar{\tau}_i' \cdot \bar{u}', \quad (6)$$

where the prime quantities are anomalies from the zonal mean. In regions of compact sea-ice, where the underlying eddy field is strong ($y = 200$ –800 km), P_i' is significantly more negative than in the rest of the ice zone, and its spatial pattern qualitatively matches that of w_{ek} . This suggests evidence of ice exerting drag upon the ocean at the mesoscale and inducing EIP.

The relatively large Rossby number of the flow ($\zeta/f \sim 0.3$) indicates that internal dynamics and wind-ocean interactions can generate significantly large vertical velocities within eddies, beyond the linear Ekman effect (Gaube et al., 2015; McGillicuddy et al., 2007; Stern, 1965; Thomas et al., 2008). This explains the filament-like structure in the diagnosed vertical velocity field (Figure 3d) evident almost everywhere, including in regions of loose sea-ice and in the open ocean.

To separate the contribution of EIP from other factors enhancing vertical velocities, we design a simulation named EIP “off”, in which the MITgcm code is modified such that the net stress felt by the ocean $\bar{\tau}$ ignores the ice-ocean stress $\bar{\tau}_i$ in Equation 4. Instead, $\bar{\tau}$ is simply set to the open-ocean wind stress $\bar{\tau}_w$, which is much more zonally symmetric. The calculation of the net stress felt by sea-ice is left unchanged. To enable comparison with the control simulation (EIP “on”), we also decrease the input magnitude of the wind speeds in the ice zone, such that the zonal mean net stresses are comparable in the EIP “on” and “off” simulations (see Figure 4). The scaled wind velocities \bar{u}_w^{sc} were calculated from the original wind velocities \bar{u}_w as follows:

$$\bar{u}_w^{sc} = (1 - \bar{\alpha}^C) \bar{u}_w, \quad (7)$$

where $\bar{\alpha}$ is the zonal mean sea-ice fraction. The exponent factor C was tuned offline to obtain a good match in the zonal mean stresses between the “on” and “off” simulations. We found that a value of $C = 10$ gives a reasonable agreement, both in the x and y directions (see Figures 4a and 4b). Large C implies that the zonal-mean stress is only significantly affected by sea-ice in regions of compact ice (high α), where the wind stress momentum is partially absorbed by sea-ice as internal stresses. When sea-ice is loose (low α), the wind transfers momentum to the ice, which in turn transfers it to the ocean without significant absorption. Panels (c–e) show how EIP enhances the scale and magnitude of the subsurface velocity in the ice zone, as quantified by a larger power in w_s for wavelengths ranging from 30 to 300 km. In what follows, we investigate the differences between the EIP “on” and “off” simulations, both at the eddy scale (Section 4) and when averaging over the compact ice zone (Section 5).

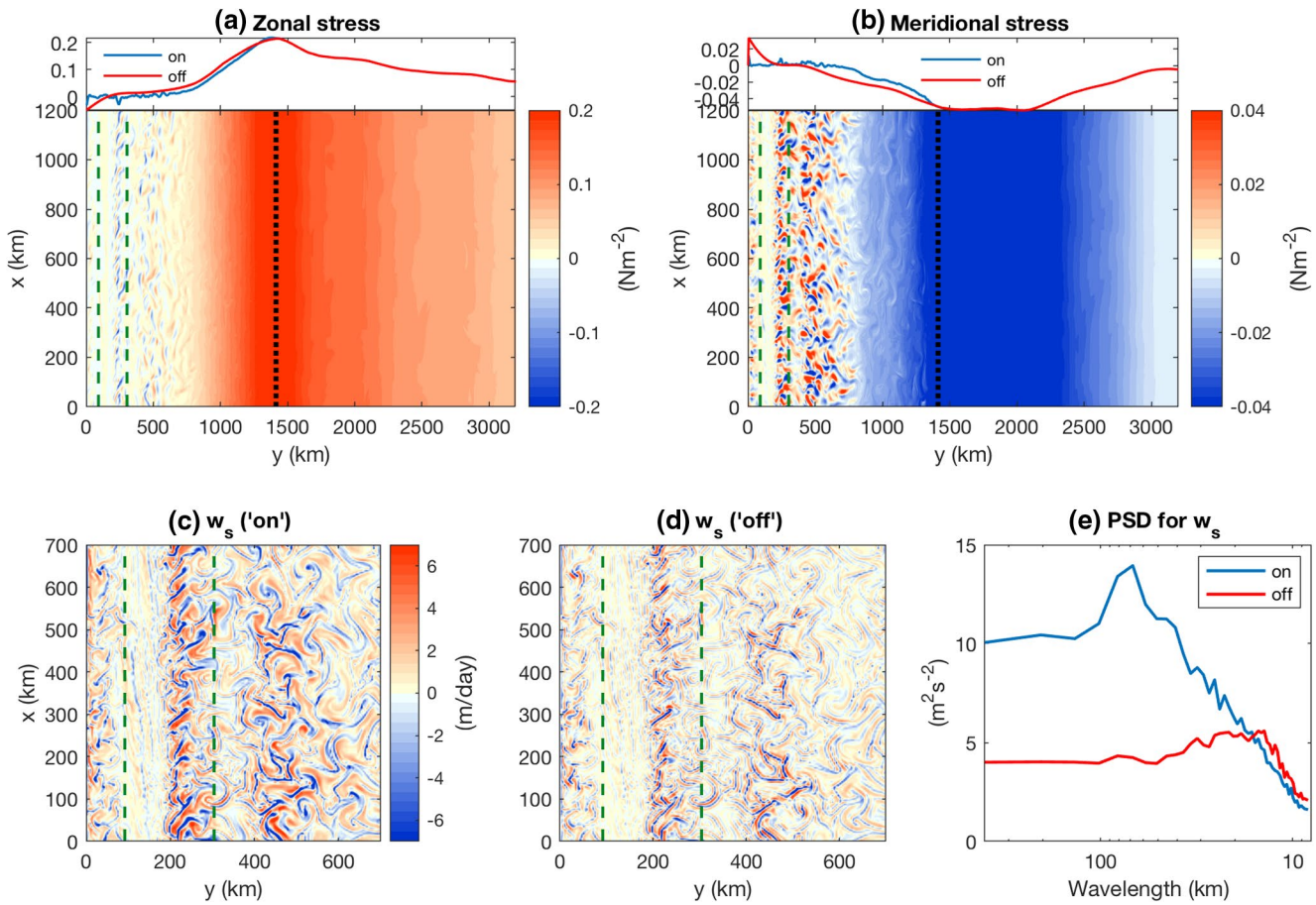


Figure 4. September snapshots of (a) the zonal and (b) the meridional stresses on the ocean surface across the whole model domain. The colored contours show the net surface stresses for the simulation where EIP is “on.” The overlaying line plots show zonal mean stresses when EIP is “on” (blue) and “off” (red). September snapshots of subsurface vertical velocity w_s within the ice zone for the cases where EIP is (c) “on” and (d) “off.” The green dashed lines indicate the edges of the continental slope and shelf respectively. The black dotted line shows the zonal mean sea-ice edge. (e) Zonal mean power spectrum density for w_s calculated between $y = 400\text{--}800$ km and plotted against the meridional wavelength.

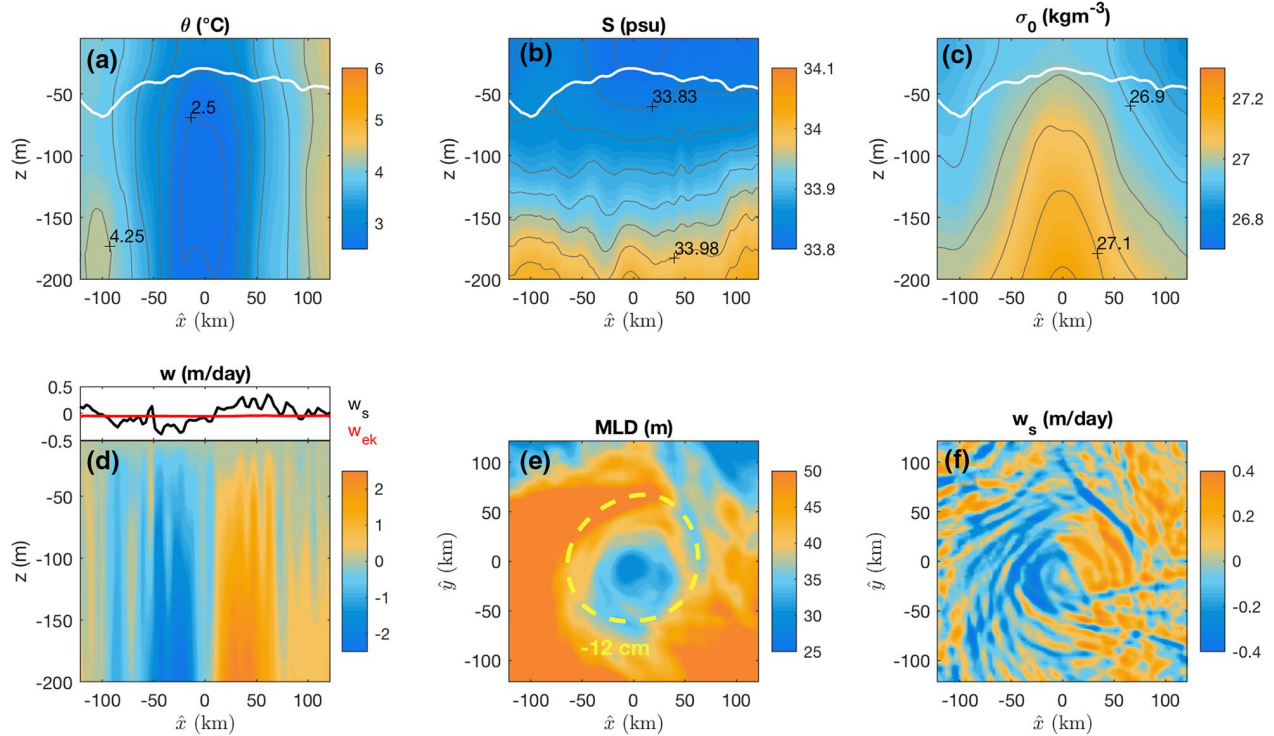
4. Eddy Detection and Compositing

In this section, we study the effects of EIP on eddies by compositing fields over cyclones and anticyclones, respectively, and averaging in the eddy-centric coordinate. Following Chelton et al. (2011), eddies are identified from closed sea surface height (SSH) anomalies and a set of criteria constraining their size and shape (as outlined in Appendix A). We detect eddies from 30 snapshots of SSH taken at 1-day interval during the month of September. The eddy size r is defined as the radius of the circle that encloses the SSH contour along which the surface current velocity is maximum (Chelton et al., 2011). The eddy-centric fields are horizontally interpolated onto a high-resolution grid spanning $-2r$ to $+2r$ in both the x and y directions. In the Southern Hemisphere, anticyclones (positive SSH) rotate counterclockwise, whereas cyclones (negative SSH) rotate clockwise. We perform the eddy composite analysis for three different cases, namely (i) the open ocean (Figure 5), (ii) the compact ice zone with EIP “on” (Figure 6), and (iii) the compact ice zone with EIP “off” (Figure 7).

4.1. Open Ocean

In the open ocean, composites are taken between $y = 1,900\text{--}2,900$ km, a region that is stratified in both temperature and salinity (see Figure 5). The composites are obtained by averaging over snapshots of 192 cyclones and 184 anticyclones, with mean sizes of 61 km for cyclones and 65 km for anticyclones, and mean

Cyclones - Open ocean



Anticyclones - Open ocean

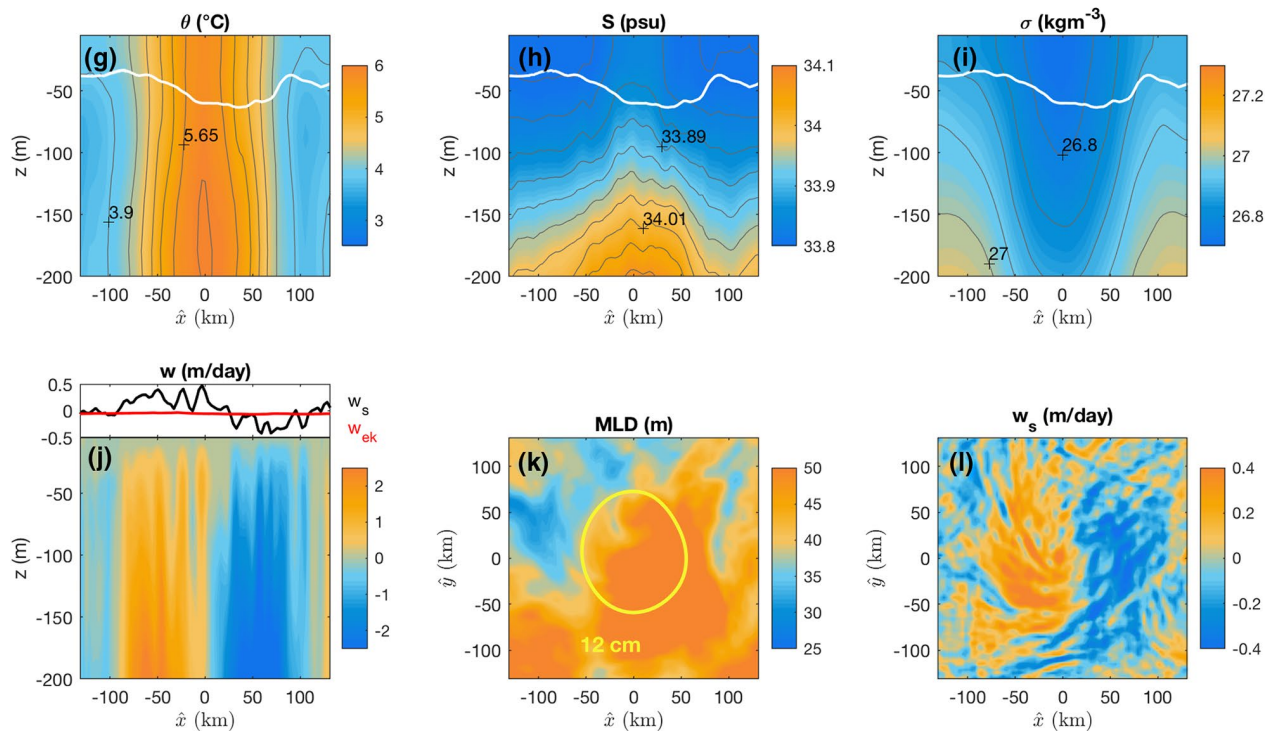


Figure 5. Open ocean composites taken between $y = 1,900\text{--}2,900$ km in the channel model for cyclones (a–f) and anticyclones (g–l) in September. The composites are projected on to a characteristic eddy radius $\hat{r} = 60$ km and the horizontal coordinates \hat{x} and \hat{y} span $-\hat{r}$ to $+\hat{r}$. The filled contours in panels (a–d) show vertical cross-sections through the center of the composite in the x -direction for θ , S , σ_t , and the vertical velocity w , respectively. The white lines in panels (a–c) indicate the MLD. The overlaying line plots in panel (d) show w_s (in black) and w_{ek} (in red). The filled contours in panels (e) and (f) show plan views of the MLD and w_s , respectively. The yellow line in panel (e) is a characteristic SSH contour. Panels (g–l) show corresponding results for the anticyclone composite.

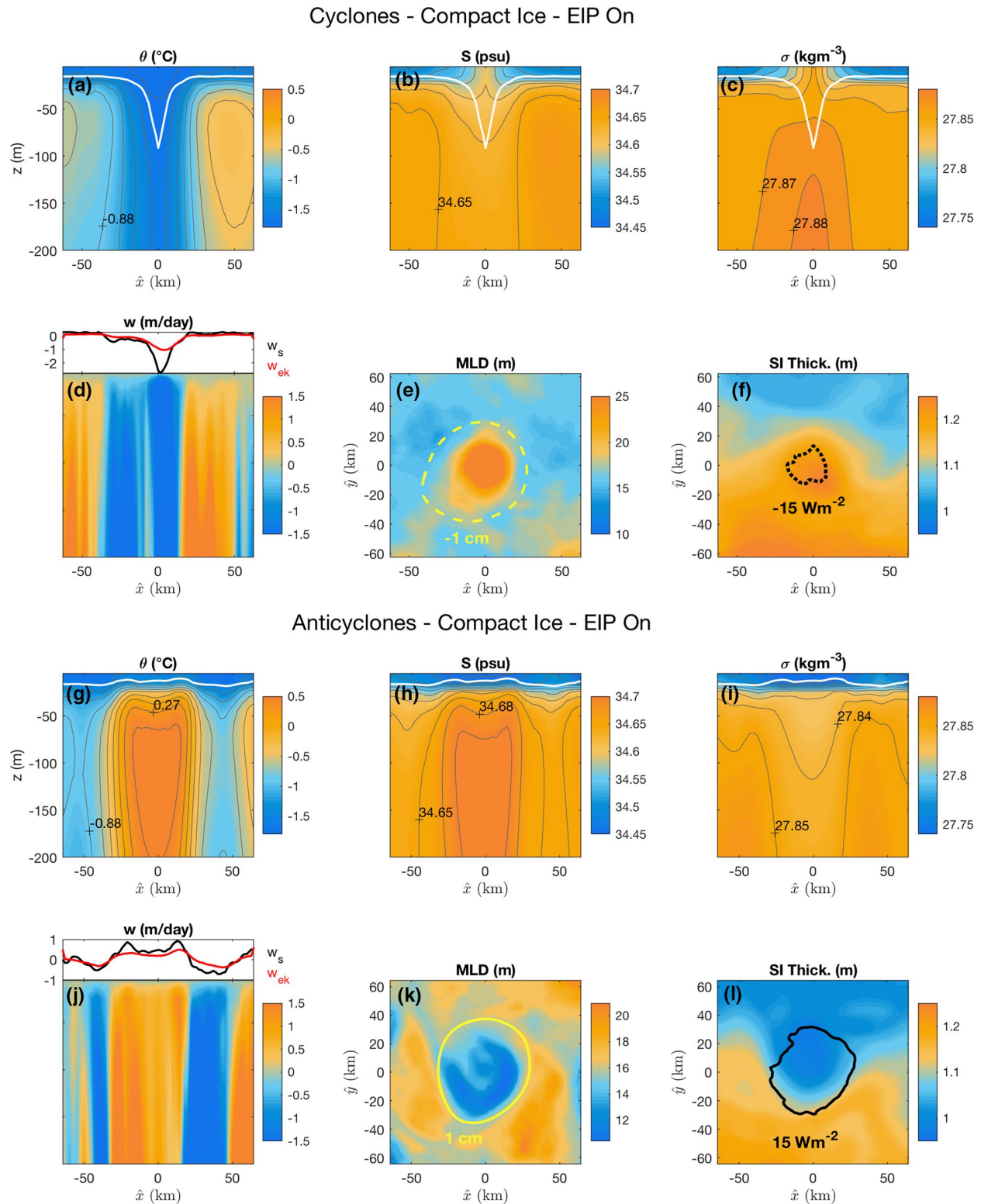
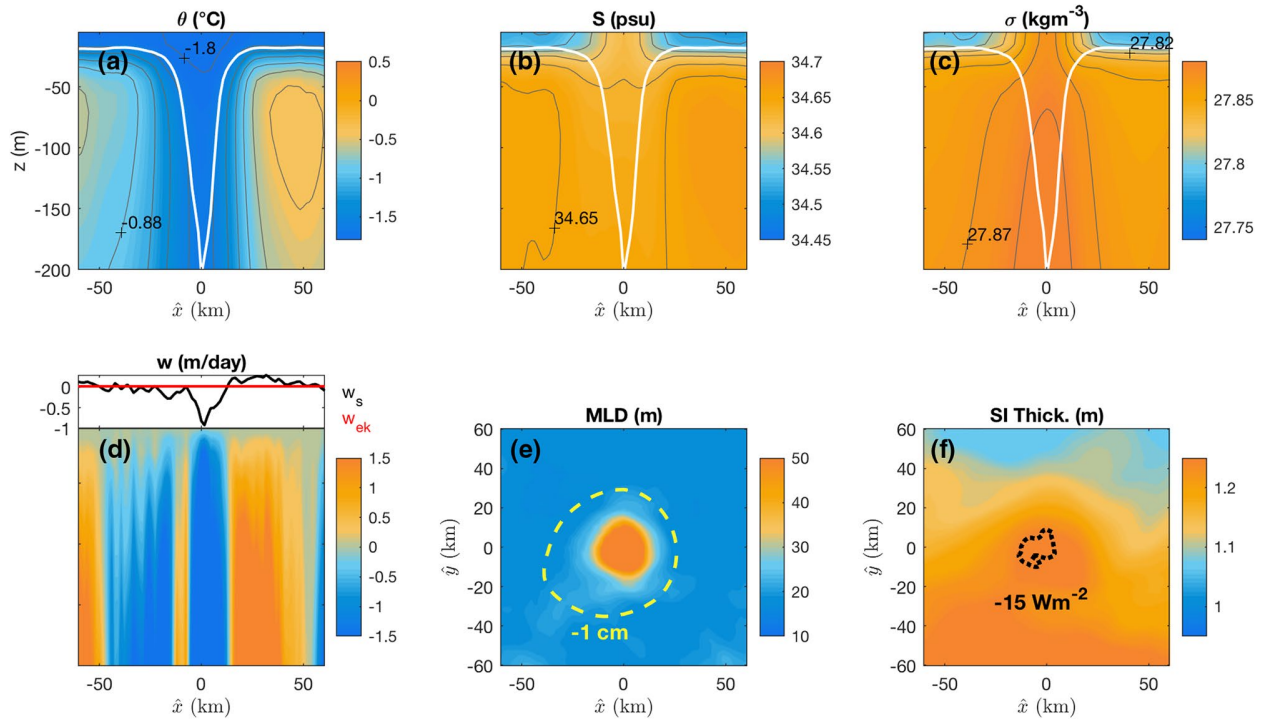


Figure 6. Compact ice zone composites with Eddy-Ice-Pumping “on” taken between $y = 400\text{--}800$ km in the channel model for cyclones (a–f) and anticyclones (g–l) in September. The composites are projected onto a characteristic eddy radius $\hat{r} = 30$ km and the horizontal coordinates \hat{x} and \hat{y} span $-2\hat{r}$ to $+2\hat{r}$. The filled contours in panels (a–d) show vertical cross-sections through the center of the composite in the x -direction for θ , S , σ_0 and the vertical velocity w , respectively. The white lines in panels (a–c) indicate the MLD. The overlaying line plots in panel (d) show w_s (in black) and w_{ek} (in red). The filled contours in panels (e) and (f) show plan views of the MLD and the area-weighted average sea-ice thickness, respectively. The yellow line in panel (e) is a characteristic SSH contour and the black line in panel (f) is a characteristic contour of the net heat flux to the ice. Panels (g–l) show corresponding results for the anticyclone composite.

Cyclones - Compact Ice - EIP Off



Anticyclones - Compact Ice - EIP Off

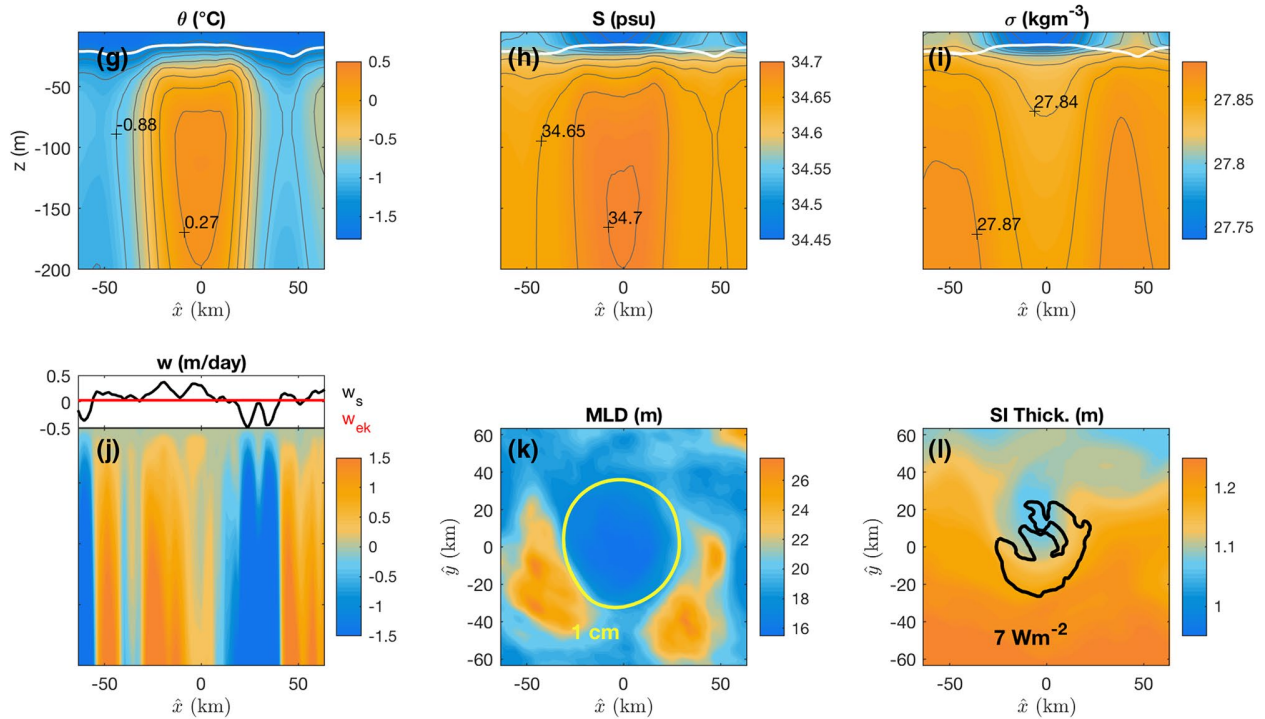


Figure 7. Compact ice zone composites with Eddy-Ice-Pumping “off” taken between $y = 400\text{--}800$ km in the channel model for cyclones (a–f) and anticyclones (g–l) in September. The composites are projected on to a characteristic eddy radius $\hat{r} = 30$ km and the horizontal coordinates \hat{x} and \hat{y} span $-2\hat{r}$ to $+2\hat{r}$. The filled contours in panels (a–d) show vertical cross-sections through the center of the composite in the x -direction for θ , S , σ_0 , and the vertical velocity w , respectively. The white lines in panels (a–c) indicate the MLD. The overlaying line plots in panel (d) show w_s (in black) and w_{ek} (in red). The filled contours in panels (e) and (f) show plan views of the MLD and the area-weighted average sea-ice thickness, respectively. The yellow line in panel (e) is a characteristic SSH contour and the black line in panel (f) is a characteristic contour of the net heat flux to the ice. Panels (g–l) show corresponding results for the anticyclone composite.

SSHs of -14 cm for cyclones and 11 cm for anticyclones. Eddies span about 30 horizontal grid points, which we consider well-resolved. The open ocean eddy characteristics found in this analysis are qualitatively consistent with the ones presented in past studies of Southern Ocean composites (Hausmann et al., 2017; Song et al., 2015).

Open ocean cyclones are characterized by a cold and fresh anomaly at their core. The isopycnals bow upwards, and the MLD conforms to that curvature, shallowing at the core of the eddy. The vertical velocity shows enhanced downwelling at the western edge of the eddy and upwelling at its eastern edge. Appendix B shows that the vertical velocity induced by eddy-wind interactions only modestly contributes to the diagnosed w_s , and that their patterns are not in phase. The process responsible for producing the dipole in w_s is not formally identified in this study, but the sign and direction of the observed patterns are consistent with isopycnal advection by eddies in a background slope. Since the mean isopycnals slope down as the latitude decreases, adiabatic poleward flow on the east of cyclones promotes upwelling, whereas equatorward flow on the west leads to downwelling. Careful analysis would be required to separate this effect from diapycnal and shear-driven vertical velocities.

Open ocean anticyclones display a mirrored structure from the cyclones. They have a warm and salty core, their isopycnals bow down, the MLD deepens, and the sign of the dipole in vertical velocity reverses. The diagnosed structure in w_s is again consistent with advection along the background isopycnal slope, generating downwelling on the eastern side of anticyclones and upwelling on their western side.

4.2. Compact Sea-Ice—EIP “on”

Figure 6 shows eddy composites taken in the compact ice zone in the simulation where EIP is “on.” The sampling domain is restricted to $y = 400$ – 800 km, since beyond $y < 400$ km, the entire water column is near the freezing temperature in September, such that the Ekman-induced vertical velocities cannot significantly affect the melting of sea-ice. For $y > 800$ km, sea-ice is too loose for EIP to play a significant role, as discussed in Section 3. In the region $y = 400$ – 800 km, the top 100 m of the water column is characterized by a temperature inversion (cold over warm) and salinity stratification (see Figure 2), whereas the rest of the column is only weakly stratified. Composites are obtained by averaging over snapshots of 231 cyclones and 174 anticyclones, with mean sizes of 31 km for cyclones and 32 km for anticyclones, and mean SSHs of -4 cm for cyclones and 4 cm for anticyclones. These eddies span about 20 horizontal grid points, roughly at the threshold between an eddy-permitting and resolving paradigm. The difference in the cyclone versus anticyclone count is only weakly significant based on a p -value of 0.05.

As in the open ocean, cyclones within the compact ice zone show a negative temperature anomaly at their core. Near the surface, the temperature is at the freezing point, which drives sea-ice formation. At the center of the cyclone, sea-ice is 0.2 m thicker than the mean (1 m), and the net heat flux to the ice is about -15 W m^{-2} (freezing). In the top 30 m, brine rejection associated with sea-ice formation causes a salty cyclone core. Between 30 and 200 m, the core is relatively fresh, as was seen in the open ocean. The edges of the cyclone show the zonal dipole in vertical velocity that was evident in the open ocean (downward motion in the west and upward motion in the east). The isopycnals bow up everywhere, but unlike in the open ocean, the MLD deepens (down to 90 m) at the center of the cyclone, driven by brine rejection. The core of the eddy exhibits downwelling due to the combined effects of EIP (red line) and brine rejection (panel d).

In anticyclones, the situation is mostly reversed from cyclones, but with some important distinctions. As in the open ocean, there is a warm temperature anomaly at the eddy core, which here tends to melt sea-ice and produce a fresh core in the top 30 m. At the center of the anticyclone, sea-ice is 0.2 m thinner than the mean (1 m), and the net heat flux to the ice is approximately $+15 \text{ W m}^{-2}$ (melting). Between 30 and 200 m, the core is saltier than the edges, as was seen in the open ocean. The edges of the anticyclone show the zonal dipole in vertical velocity that was evident in the open ocean (upward motion in the west and downward motion in the east). The isopycnals bow down everywhere, but unlike in the open ocean, the MLD is anomalously shallow at the core, due to increased stratification from sea-ice melt. The warm and salty properties of the eddy are enhanced by upwelling at the core bringing deeper waters up to the surface. We argue that this

upward motion is favored by EIP, as evidenced by the good match between w_s (black line) and w_{ek} (red line) shown in panel (j).

4.3. Compact Sea-Ice—EIP “off”

To assess the effect of EIP on eddy structures, we again take composites in the compact ice zone between $y = 400\text{--}800$ km, but now in the simulation where EIP is “off” (see Figure 7). The composite mean is obtained by averaging over snapshots of 259 cyclones and 218 anticyclones, with mean sizes of 31 km for cyclones and 32 km for anticyclones, and mean SSHs of -4 cm for cyclones and 4 cm for anticyclones. The difference in the cyclone versus anticyclone count is not statistically significant based on a p -value of 0.05.

The composited cyclone profiles are similar between the EIP “on” and “off” cases. The surface temperature is still near freezing and both the ice thickness and the net heat flux to the ice are unchanged from the EIP “on” simulation. The Ekman pumping velocity is zero (red line in panel d), and the diagnosed surface downwelling velocity at the core (black line in panel d) is lower than in the EIP “on” case (1 m/day instead of 2 m/day). Brine rejection again drives downward velocity at the core and deepens the MLD within the cyclone. However, the MLD is deeper when EIP is “off” (down to 200 m) because weaker downwelling reduces the distribution of brine rejected waters into deeper layers, decreasing $\Delta\sigma$ and hence deepening the MLD.

In anticyclones, the Ekman suction velocity is now zero (red line in panel d), hence the vertical velocity at the eddy core is weak. Instead, the w profile looks similar to that found in the open ocean, with the zonal dipole at the eddy edges. The lack of upward motion at the eddy center limits the amount of warm waters brought up to the surface, which reduces the temperature of the eddy core by approximately 0.1°C relative to the EIP “on” case. The sea-ice thickness is only 0.1 m thinner than the mean, and the net heat flux acting to melt sea-ice is $+7\text{ W m}^{-2}$ (compared to 0.2 m and $+15\text{ W m}^{-2}$, respectively, in the EIP “on” case). The MLD still shallows at the eddy core, but slightly less than when EIP is “on,” due to reduced sea-ice melt.

In summary, we find that anticyclones are sites of sea-ice melt, with a correspondingly shallow MLD (~ 20 m). The net effect of EIP on anticyclones is to upwell warm waters to the surface, which enhances sea-ice melt. On the other hand, cyclones are sites of sea-ice formation, with relatively deeper MLDs ($\sim 30\text{--}200$ m). In these eddies, EIP enhances downwelling at the eddy core but does not alter sea-ice formation. This is fundamentally due to the lower threshold imposed by the freezing point on ocean temperature, such that the cyclone surface is near the freezing point with or without EIP, and the net ocean-to-ice heat flux is virtually unchanged.

5. Aggregate Effects of Eddy-Ice Interactions

In this section, we investigate whether the anomalous melt in anticyclones caused by EIP can have any significant aggregate effect on the system's mean state. Figure 8 shows the seasonal evolution of zonal mean heat fluxes and sea-ice thickness evaluated within the compact ice zone ($y = 400\text{--}800$ km) over 1 year of the simulation. We calculate the vertical heat flux H at the surface as:

$$H = \rho_0 c_w w_s \theta_s, \quad (8)$$

where both w_s and θ_s are diagnosed at the first vertical model layer. We decompose H into its mean ($\bar{H} = \rho_0 c_w \bar{w}_s \bar{\theta}_s$) and eddying ($H' = \rho_0 c_w w'_s \theta'_s$) components, where deviations are taken from the zonal mean. We also consider the net heat absorbed or provided by sea-ice from its surroundings for melt or formation, respectively.

In the control simulation (EIP “on”), Figure 8 shows that sea-ice formation occurs mostly between April and July, and sea-ice melt from September to March. The mean sea-ice thickness grows from 0 to 1.2 m between February and June and stays approximately constant until November. EIP enhances the net vertical heat fluxes toward the ice, particularly between August and October (an increase of approximately $3\text{--}5\text{ W m}^{-2}$). The increase in H is mostly driven by the eddying component H' , as expected from EIP. The enhanced

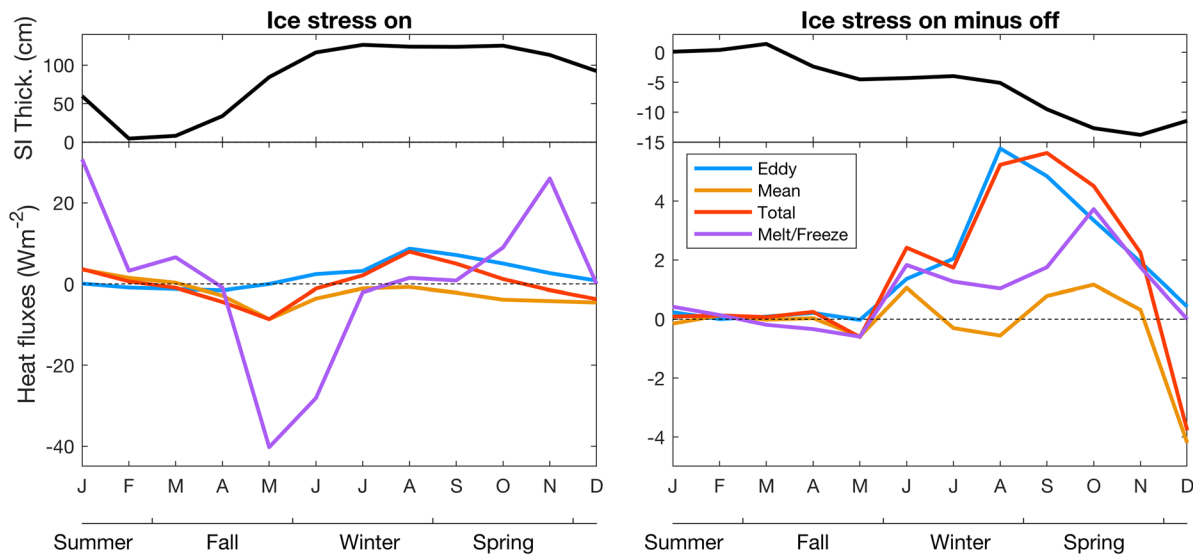


Figure 8. Seasonal evolution of the area-weighted average sea-ice thickness (top) and heat fluxes (bottom) within the compact ice zone ($y = 400\text{--}800$ km) calculated for the first year of the sensitivity simulation. (left) EIP “on” and (right) EIP “on” minus “off.”

upward heat flux is reflected in the melting rate, which increases by $2\text{--}4\text{ W m}^{-2}$ during those months. Consequently, the mean sea-ice thickness decreases by 13 cm (about 10%) over the course of winter and spring.

In Figure 9, we investigate the seasonal effects of EIP on mean vertical profiles within the compact ice zone ($y = 400\text{--}800$ km), by comparing the simulations with EIP “on” and “off.” In the control run, θ remains around -1°C for the whole year below 40 m depth. In the top 40 m, the temperature varies seasonally up to 1°C in summer and down to freezing (-1.8°C) in winter and spring. The salinity below 40 m depth is 34.7 psu year-round, but varies seasonally between 34.7 psu (in winter and spring) and 33.5 psu (in summer and fall) in the top 40 m. The N^2 profile has a peak around 20 m depth that is strongest in summer and fall, weak in spring, and absent in winter. The EKE profiles have a peak around 20–50 m depth, but otherwise decrease monotonically with depth. Near the surface, EKE tends to be slightly larger in winter and spring compared to summer and fall.

The difference between the EIP “on” and “off” simulations shows warming on the order of 0.15°C between 20 and 40 m depth during winter and spring, consistent with EIP bringing warm waters up closer to the surface during those months. The top 20 m is only marginally warmer, likely due to some of the upwelled heat transferred to the atmosphere and the ice. EIP only has a marked effect on salinity in spring, during which the top 30 m freshens by approximately 0.04 psu, driven by sea-ice melt. This near-surface warming and freshening increases the peak in stratification at 20 m depth. The dissipation of oceanic energy against sea-ice tends to decrease EKE throughout the water column in spring, but not during the other seasons.

As was shown in Figure 8, EIP warms the subsurface ocean and drives anomalous sea-ice melt during winter and spring, when averaged over the compact ice zone. This lightens the surface ocean and shoals the MLD by up to 20 m (60%) between May and October (see Figure 10), consistent with results found for cyclonic and anticyclonic eddies during the month of September (see Figures 6 and 7). Anomalous sea-ice formation immediately follows between November and January, such that the effect of EIP does not build up over the years, but follows a regular seasonal cycle (Figure 10d). The recovery and overshoot in sea-ice thickness is possibly the result of a negative feedback, whereby increased surface stratification following sea-ice melt facilitates surface cooling and sea-ice formation (D. G. Martinson, 1990; McPhee et al., 1999; Wilson et al., 2019). EIP brings up warm and salty waters near the surface between May and October (panels a and b), which causes sea-ice melt during those months and surface freshening between September and December. Panel (d) shows anomalous heat flux out of the ocean between July and the following February, suggesting that the warm SSTs caused by EIP draws anomalous cooling from the atmosphere, which could also contribute to ice thickness recovery. The MLD anomaly also follows a regular seasonal cycle, shoaling

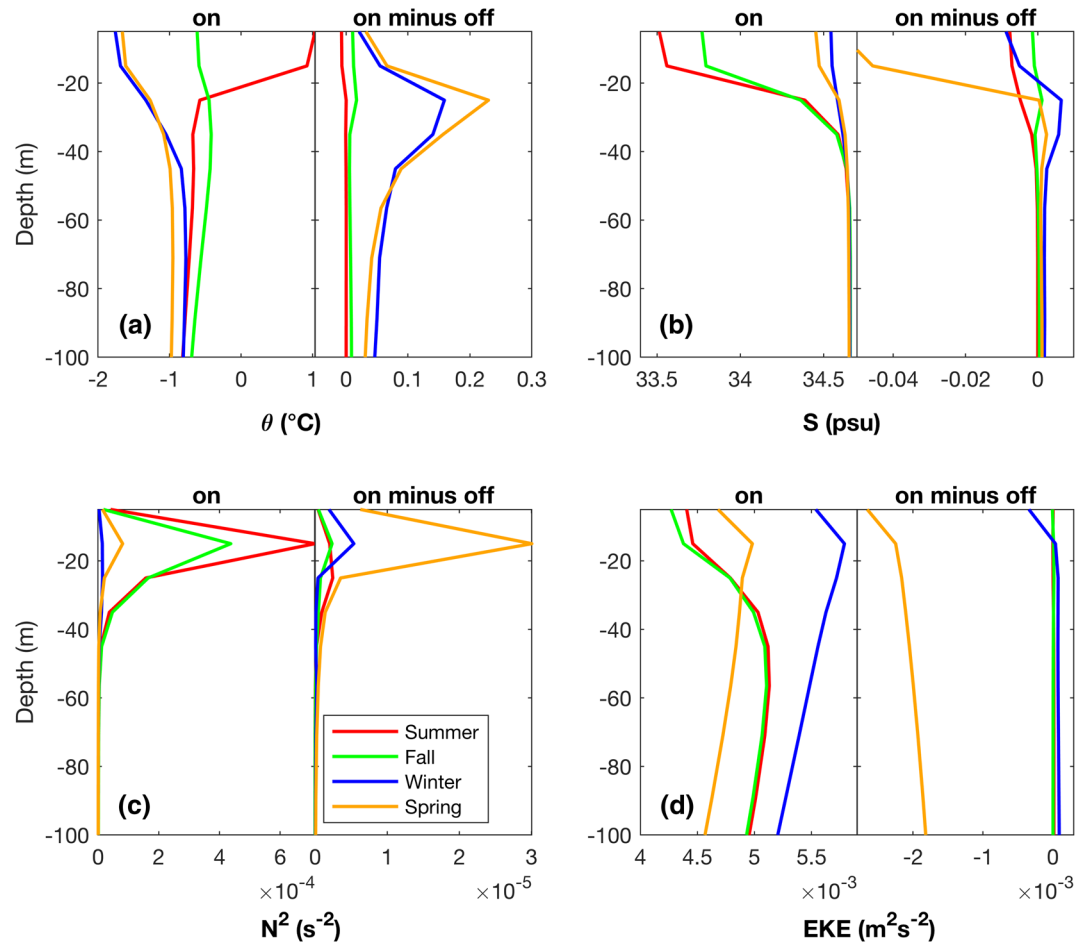


Figure 9. Vertical profiles of (a) θ , (b) S , (c) N^2 , and (d) EKE within the compact ice zone ($y = 400\text{--}800$ km, zonal mean) calculated for the first year of the sensitivity simulation and averaged over seasons: summer in red (JF), fall in green (MAM), winter in blue (JJA), and spring in orange (SON). The left panel of each subplot shows Eddy-Ice-Pumping “on” and the right panel shows “on” minus “off.”

in winter and recovering by the end of spring. In summer and fall, the MLD is shallow, and the $\Delta\sigma$ anomalies are too deep to significantly affect it (not shown).

6. Discussion and Conclusions

In polar oceans, the seasonal ice zone typically displays a subsurface temperature inversion, whereby a cold and fresh lens shields sea-ice from underlying warm and salty waters. In the Southern Ocean, warm UCDWs upwell below the surface layer and provide a heat reservoir for sea-ice melt (Ackley et al., 2015). The relatively weak density stratification in these Antarctic regions affords significant importance to vertical heat exchanges driven by small-scale processes underneath the ice (Martinson & Iannuzzi, 1989; McKee et al., 2019). This study presents a mechanism, dubbed EIP, by which the frictional coupling between sea-ice and the ocean below can bring warm waters up to the surface and promote melting in the compact ice zone. In regions of densely packed sea-ice, mesoscale eddies feel surface drag from the relatively stationary ice, which generates vertical Ekman velocities and mixes the water column. Numerical simulations in an eddy channel model of the Southern Ocean show that in areas where the sea-ice fraction is higher than about 80%, EIP drives upwelling in anticyclones and downwelling in cyclones, with magnitudes on the order of $1\text{--}10$ m day⁻¹. The integrated effect of EIP in our simulations is that of net surface warming because it raises

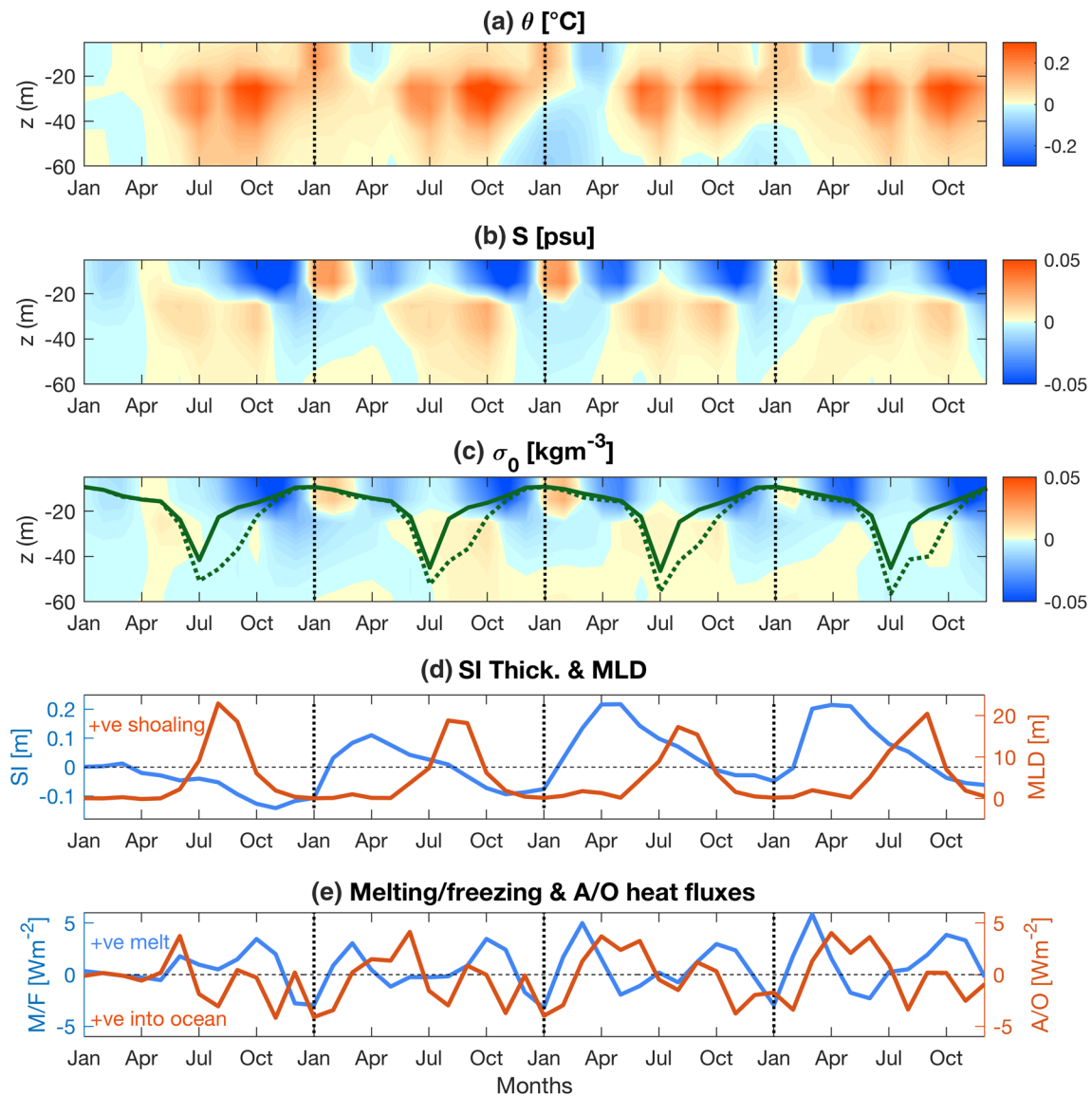


Figure 10. Four-year evolution of the EIP “on” minus “off” simulations averaged within the compact ice zone ($y = 400\text{--}800$ km) for (a) θ , (b) S , (c) σ_0 , (d) area-weighted average sea-ice thickness (blue) and MLD (red), (e) net heat flux from the atmosphere to the ocean (red) and net heat flux to sea-ice (blue). The vertical dotted lines separate each individual year. The green lines in panel (c) indicate the MLD for EIP “on” (solid) and “off” (dashed).

the temperature beneath the ice in anticyclones without significantly affecting cyclones, whose temperature is already at the freezing point.

In the compact ice zone, EIP reduces sea-ice thickness by 13 cm (10%) between May and November, due to anomalously large vertical eddy heat fluxes at the surface that peak to 6 W m^{-2} in September and October. In spring, anomalous sea-ice melt increases stratification in the near-surface layers of the ocean, shoaling the MLD by up to 20 m (60%). Mechanical drag from ice also reduces EKE throughout the water column. The sea-ice thickness recovers (with an overshoot) the following summer and fall, such that the effect of EIP does not accumulate over the years, but only changes the seasonality of sea-ice and MLD. This recovery is likely facilitated by the negative feedback between surface stratification and sea-ice melt (D. G. Martinson, 1990; McPhee et al., 1999; Wilson et al., 2019), and the fact that warmer SSTs draw anomalous cooling from the atmosphere between July and March.

The EIP interactions described in this study are analogous to aspects of eddy-wind interactions observed in the open ocean (Gaube et al., 2015; McGillicuddy, 2016; McGillicuddy et al., 2007; Seo, 2017; Song et al., 2020; Zhai et al., 2012). At relatively high Rossby numbers, eddies subjected to a large scale wind stress develop a dipole in vertical velocity to balance a vortex tilting tendency (Niiler, 1969; Stern, 1965). Moreover, the differential enhancement of surface stress on opposite sides of an eddy may drive a monopole in Ekman vertical velocity at the core of the vortex (Dewar & Flierl, 1987). In our simulations, open ocean eddy-wind interactions produce a negligible monopole, and a dipole that only has a modest impact on the vertical velocity w . In the compact ice zone, eddy-wind interactions are also weak, while EIP generates a strong monopole that significantly enhances w . The strength of this monopole reflects the higher effectiveness of EIP in generating an eddy-scale stress curl in regions of pack ice, as compared to large scale winds.

Another distinguishing factor of eddies in the compact ice zone is the thermodynamic modulation of MLDs from sea-ice melting and freezing. In the open ocean, eddies can modulate the MLD through the vertical displacement of isopycnals associated with eddy formation and decay. Our open ocean composites show a deepening of the MLD in anticyclones and a shoaling in cyclones, consistent with previous work (Hausmann et al., 2017; Song et al., 2015). In the compact ice zone, however, the MLD shallows in anticyclones due to sea-ice melt (~ 20 m), and deepens in cyclones (~ 50 – 200 m) due to brine rejection from sea-ice formation. The latter is consistent with the deepening of MLDs observed by Charrassin et al. (2008) for Antarctic MLDs subjected to brine rejection under sea-ice in winter/spring. Furthermore, EIP shoals the MLD via increased sea-ice melt in anticyclones, and via increased transport of brine waters into deeper layers in cyclones. The effects of EIP and ice melt/formation on MLD may have important consequences for tracer transport, nutrient cycling, and biological activity in the compact ice region (McGillicuddy et al., 1998; Williams & Follows, 1998).

On the large scale, winds typically impart momentum to sea-ice, which in turn accelerates the mean currents. However, EIP may extract momentum at smaller scales, when sea-ice is stationary relative to underlying mesoscale eddies. In regions of loose sea-ice, internal ice stresses are too weak to resist the eddy motion, and the local difference in ice/ocean velocities is too small for there to be a significant eddy-scale drag. Manucharyan and Thompson (2017) argue that in the Arctic MIZ, in the absence of winds and sea-ice thermodynamics, cyclonic eddies and filaments effectively trap sea-ice due to converging motion at the surface, while anticyclones repel ice due to local divergence. The resulting asymmetry in ice thickness could perhaps be enhanced by the effects of sea-ice melt and freeze discussed in our study, as cyclones are typically cold and anticyclones warm. Moreover, the horizontal density gradients observed across eddies in our compact ice zone could trigger submesoscale activity that is currently not resolved in our model. These fine scale processes may generate vertical velocities on the order of 10–100 m/day, which could significantly impact local heat fluxes, depending on their coherence and persistence (Boccaletti et al., 2007; Manucharyan & Thompson, 2017; Thomas et al., 2008). Some of our results may also be sensitive to the specific sea-ice and mixing parameterizations used in our model, particularly those relating to ice/ocean stress, brine rejection, and vertical exchanges. This warrants further investigations with higher resolution models and observations. Finally, it remains to be shown whether EIP can occur in the Arctic basin, where sea-ice, stratification, and eddy characteristics differ from the Antarctic.

Appendix A: Eddy Detection Procedure

Eddies are identified based on the following algorithm, based on Chelton et al. (2011) and Song et al. (2015):

1. Find closed contours in sea surface height anomaly
2. Check that the closed contours have more than the minimum number of pixels (75 in the compact ice zone and 500 in the open ocean)
3. Check that there is only one extremum within the closed contours
4. Check that the amplitude is larger than the minimum threshold (4 cm in the open ocean and 2.5 cm in the compact ice zone)
5. Compute the maximum distance between pixels and check that it does not exceed a threshold value (180 px in the open ocean and 100 px in the compact ice zone). This ensures that the eddy shapes are not too different from circles

The parameter values used in the open ocean are similar to those reported in Song et al. (2015) and the composite results are not highly sensitive to these choices. In the compact ice zone, eddies are typically smaller and weaker than in the open ocean, so parameters were adapted empirically to produce reasonable composites. Note that the SSH takes account of the displacement caused by the weight of sea-ice.

Appendix B: Eddy-Wind Interactions

Eddy-wind interactions modulate both the wind stress and its curl, which can locally enhance vertical velocities through Ekman processes. When the Rossby number is not negligible, there is a non-linear component to the vertical velocity that tends to balance vortex tilting (Niiler, 1969; Song et al., 2020; Stern, 1965;

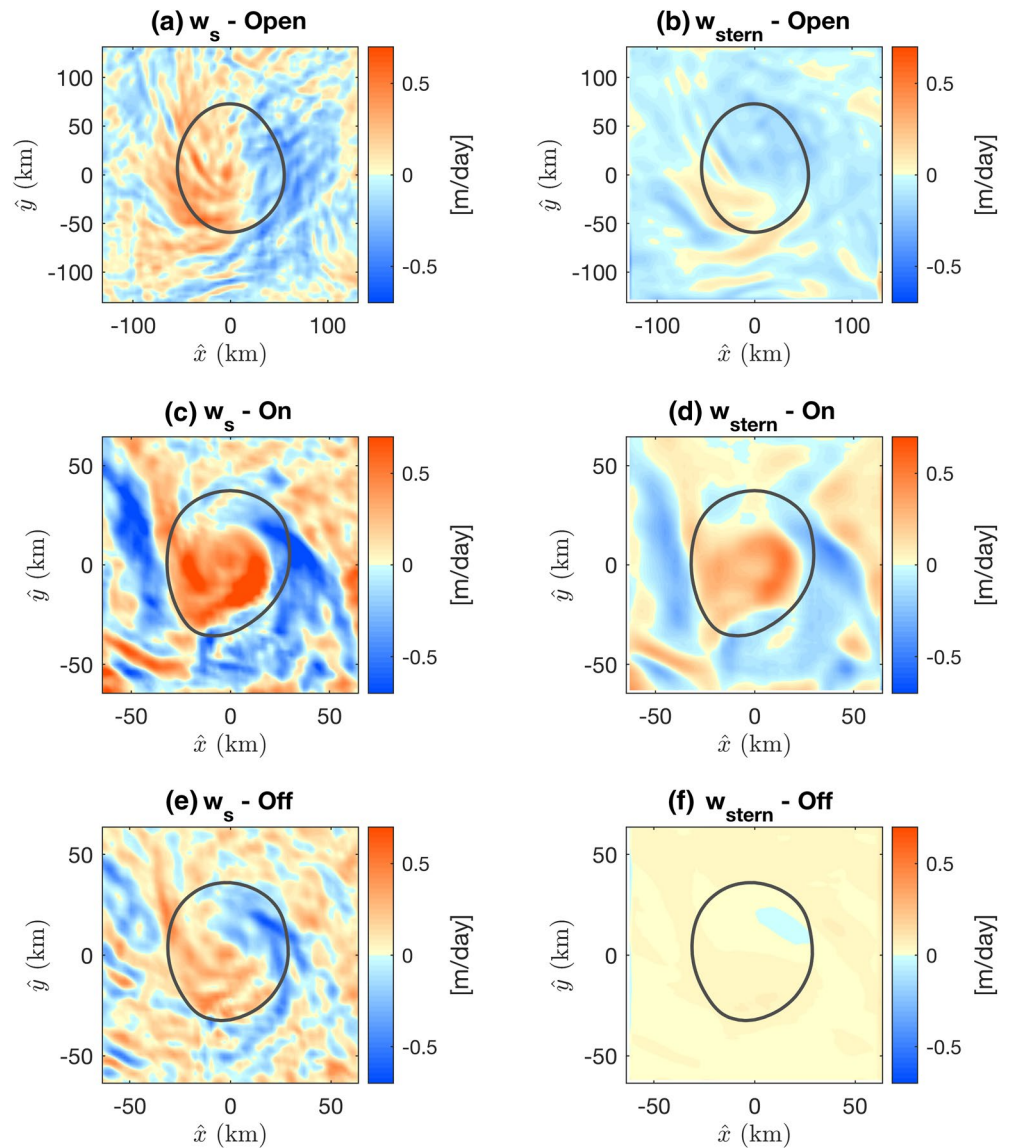


Figure B1. Composite means of anticyclones for w_s (left) and w_{stern} (right). The composites are taken in the open ocean (top), in the compact ice zone with EIP “on” (middle) and in the compact ice zone with the EIP “off” (bottom). The gray contours indicate characteristic sea surface heights at values of +12 cm in the open ocean (panels a and b) and +1 cm in the ice zone panels (c-f).

Wenegrat & Thomas, 2017). Stern (1965) derives the following expression for the total Ekman pumping velocity w_{stern} as follows:

$$\begin{aligned} w_{\text{stern}} &\approx w_{\text{curl}} + w_{\zeta} \\ &= \frac{\nabla \times \bar{\tau}}{\rho_0(f + \zeta)} + \frac{\bar{\tau} \times \nabla \zeta}{\rho_0(f + \zeta)^2} \\ &= \frac{\nabla \times \bar{\tau}}{\rho_0(f + \zeta)} + \frac{1}{\rho_0(f + \zeta)^2} \left(\tau_x \frac{\partial \zeta}{\partial y} - \tau_y \frac{\partial \zeta}{\partial x} \right), \end{aligned} \quad (\text{B1})$$

where w_{curl} is the linear Ekman velocity term and w_{ζ} is the non-linear interaction term. Perpendicular to a uniform wind stress $\bar{\tau}$, the differential enhancement of stress on either side of an eddy can generate a monopole in Ekman suction/pumping at the core of the vortex due to w_{curl} . Additionally, when ζ is not negligible, w_{ζ} produces a dipole pattern in the direction perpendicular to $\bar{\tau}$.

We consider composites of anticyclones for w_{stern} and the subsurface velocity w_s (Figure B1). In the open ocean, w_{stern} has a dipole pattern mostly aligned with the meridional direction, consistent with w_{ζ} dominating over w_{curl} , and with winds being predominantly zonal (panels a and b). w_{stern} only contributes modestly to w_s , whose dipole is stronger and in the zonal direction. In the compact ice zone, when EIP is “on,” w_{stern} matches the pattern in w_s better, but does not completely account for it (panels c and d). When EIP is “off,” w_{stern} is negligible, which suggests that the pattern shown in panel (d) is dominated by ice-ocean stresses rather than eddy-wind interactions. We thus conclude that eddy-wind interactions contribute only weakly to the vertical velocity profile of anticyclones, both in the open ocean and in the ice zone. Similar results are obtained for cyclones (not shown).

Data Availability Statement

The MITgcm configuration files used in this study are available at <http://doi.org/10.5281/zenodo.3827532>.

Acknowledgments

Mukund Gupta and John Marshall acknowledge support from the NSF Antarctic Program, Hajoong Song acknowledges the support of the National Research Foundation of Korea (NRF) grant funded by the Korean government (MSIT; NRF-2019R1C1C1003663) and the Yonsei University Research Fund of 2020-22-0114, Jean-Michel Campin acknowledges support from the MIT-GISS collaborative agreement, and Gianluca Meneghello acknowledges support from the NSF program on Arctic Research (1603557). We are grateful for the insightful reviews provided by Georgy Manucharyan and Chris Horvat that helped improved the manuscript.

References

- Ackley, S. F., Xie, H., & Tichenor, E. A. (2015). Ocean heat flux under Antarctic sea ice in the Bellingshausen and Amundsen Seas: Two case studies. *Annals of Glaciology*, 56(69), 200–210. <https://doi.org/10.3189/2015AoG69A890>
- Adcroft, A., Hill, C., & Marshall, J. (1997). Representation of topography by shaved cells in a height coordinate ocean model. *Monthly Weather Review*, 125(9), 2293–2315. [https://doi.org/10.1175/15200493\(1997\)125<2293:ROTBSC>2.0.CO;2](https://doi.org/10.1175/15200493(1997)125<2293:ROTBSC>2.0.CO;2)
- Boccaletti, G., Ferrari, R., & Fox-Kemper, B. (2007). Mixed layer instabilities and restratification. *Journal of Physical Oceanography*, 37(9), 2228–2250. <https://doi.org/10.1175/JPO3101.1>
- Carmack, E., Polyakov, I., Padman, L., Fer, I., Hunke, E., Hutchings, J., et al. (2015). Toward quantifying the increasing role of oceanic heat in sea ice loss in the new Arctic. *Bulletin of the American Meteorological Society*, 96(12), 2079–210. <http://doi.org/10.1175/BAMS-D-13-00177.1>
- Charrassin, J.-B., Hindell, M., Rintoul, S. R., Roquet, F., Sokolov, S., Biuw, M., et al. (2008). Southern Ocean frontal structure and sea-ice formation rates revealed by elephant seals. *Proceedings of the National Academy of Sciences*, 105(33), 11634–11639. <https://doi.org/10.1073/pnas.0800790105>
- Chelton, D. B., Schlax, M. G., & Samelson, R. M. (2011). Global observations of nonlinear mesoscale eddies. *Progress in Oceanography*, 91(2), 167–216. <https://doi.org/10.1016/j.pocean.2011.01.002>
- Dewar, W. K., & Flierl, G. R. (1987). Some effects of the wind on rings. *Journal of Physical Oceanography*, 17(10), 1653–1667. [https://doi.org/10.1175/1520-0485\(1987\)017<1653:SEOTWO>2.0.CO;2](https://doi.org/10.1175/1520-0485(1987)017<1653:SEOTWO>2.0.CO;2)
- Doddridge, E. W., Marshall, J., Song, H., Campin, J., Kelley, M., & Nazarenko, L. (2019). Eddy compensation dampens Southern Ocean sea surface temperature response to westerly wind trends. *Geophysical Research Letters*, 46(8), 4365–4377. <https://doi.org/10.1029/2019GL082758>
- Gaspar, P., Grégoris, Y., & Lefevre, J.-M. (1990). A simple eddy kinetic energy model for simulations of the oceanic vertical mixing: Tests at station Papa and long-term upper ocean study site. *Journal of Geophysical Research*, 95(C9), 16179–16193. <https://doi.org/10.1029/JC095iC09p16179>
- Gaube, P., Chelton, D. B., Samelson, R. M., Schlax, M. G., & O’Neill, L. W. (2015). Satellite observations of mesoscale eddy-induced Ekman pumping. *Journal of Physical Oceanography*, 45(1), 104–132. <https://doi.org/10.1175/JPO-D578-14-0032.1>
- Geiger, C. A., Ackley, S. F., & Hibler, W. D., III (1998). Sea ice drift and deformation processes in the Western Weddell Sea. In M. O. Jeffries (Ed.), *Antarctic sea ice: Physical processes, interactions and variability* (pp. 141–160). Washington, DC: American Geophysical Union (AGU). <https://doi.org/10.1029/AR074p0141>
- Hausmann, U., McGillicuddy, D. J., & Marshall, J. (2017). Observed mesoscale eddy signatures in Southern Ocean surface mixed-layer depth: Southern Ocean eddy mixed-layer depths. *Journal of Geophysical Research: Oceans*, 122(1), 617–635. <https://doi.org/10.1002/2016JC012225>
- Holte, J., & Talley, L. (2009). A new algorithm for finding mixed layer depths with Applications to Argo data and subantarctic mode water formation*. *Journal of Atmospheric and Oceanic Technology*, 26(9), 1920–1939. <https://doi.org/10.1175/2009JTECHO543.1>

- Hunke, E. C., & Dukowicz, J. K. (1997). An elastic-viscous-plastic model for sea ice dynamics. *Journal of Physical Oceanography*, 27(9), 1849–1867. [https://doi.org/10.1175/1520-0485\(1997\)027<1849:AEVPMF>2.0.CO;2](https://doi.org/10.1175/1520-0485(1997)027<1849:AEVPMF>2.0.CO;2)
- Hunkins, K. L. (1981). *Arctic Ocean eddies and baroclinic instability* (Tech. Rep. 598). Palisades, NY: Lamont-Doherty Geology Observations of Columbia University.
- Jackett, D. R., & McDougall, T. J. (1995). Minimal Adjustment of hydrographic profiles to Achieve static stability. *Journal of Atmospheric and Oceanic Technology*, 12(2), 381–389. [https://doi.org/10.1175/1520-0426\(1995\)012<0381:MAOHT>2.0.CO;2](https://doi.org/10.1175/1520-0426(1995)012<0381:MAOHT>2.0.CO;2)
- Jackson, J. M., Williams, W. J., & Carmack, E. C. (2012). Winter Sea-ice melt in the Canada Basin, Arctic Ocean. *Geophysical Research Letters*, 39(3), 1–6. <https://doi.org/10.1029/2011GL050219>
- Johannessen, O. M., Johannessen, J. A., Svendsen, E., Shuchman, R. A., Campbell, W. J., & Josberger, E. (1987). Ice-edge eddies in the Fram Strait marginal ice zone. *Science*, 236(4800), 427–429. <https://doi.org/10.1126/science.236.4800.427>
- Large, W. G., & Pond, S. (1982). Sensible and latent heat flux measurements over the ocean. *Journal of Physical Oceanography*, 12(5), 464–482. [https://doi.org/10.1175/1520-0485\(1982\)012<0464:SALHFM>2.0.CO;2](https://doi.org/10.1175/1520-0485(1982)012<0464:SALHFM>2.0.CO;2)
- Large, W. G., & Yeager, S. G. (2009). The global climatology of an interannually varying air–sea flux data set. *Climate Dynamics*, 33(2), 341–364. <https://doi.org/10.1007/s00382-008-0441-3>
- Lenn, Y. D., Wiles, P. J., Torres-Valdes, S., Abrahamsen, E. P., Rippeth, T. P., Simpson, J. H., et al. (2009). Vertical mixing at intermediate depths in the Arctic boundary current. *Geophysical Research Letters*, 36(5), 1–5. <https://doi.org/10.1029/2008GL036792>
- Locarnini, R. A., Mishonov, A. V., Antonov, J. I., Boyer, T. P., Garcia, H. E., Baranova, O. K., et al. (2013). World ocean atlas 2013. Volume 1, Temperature. NOAA atlas NESDIS; 73. National Oceanographic Data Center (U.S.), Ocean Climate Laboratory and United States, Data, and Information Service, National Environmental Satellite. <https://doi.org/10.7289/V55X26VD>
- Losch, M., Menemenlis, D., Campin, J.-M., Heimbach, P., & Hill, C. (2010). On the formulation of sea-ice models. Part 1: Effects of different solver implementations and parameterizations. *Ocean Modelling*, 33(1), 129–144. <https://doi.org/10.1016/j.ocemod.2009.12.008>
- Manley, T. O., & Hunkins, K. (1985). Mesoscale eddies of the Arctic ocean. *Journal of Geophysical Research*, 90(1974), 4911–4930.
- Manucharyan, G. E., & Thompson, A. F. (2017). Submesoscale sea ice–ocean interactions in marginal ice zones. *Journal of Geophysical Research: Oceans*, 122(12), 9455–9475. <https://doi.org/10.1002/2017JC012895>
- Marshall, J., Adcroft, A., Hill, C., Perelman, L., & Heisey, C. (1997a). A finite-volume, incompressible Navier Stokes model for studies of the ocean on parallel computers. *Journal of Geophysical Research*, 102(C3), 5753–5766. <https://doi.org/10.1029/96JC02775>
- Marshall, J., Hill, C., Perelman, & Adcroft, A. (1997b). Hydrostatic, quasi-hydrostatic, and non-hydrostatic ocean modelling. *Journal of Geophysical Research*, 102(C3), 5733–5752. <https://doi.org/10.1029/96JC02776>
- Martinson, D. G. (1990). Evolution of the Southern Ocean winter mixed layer and sea ice: Open ocean Deepwater formation and ventilation. *Journal of Geophysical Research*, 95(C7), 11641–11654. <https://doi.org/10.1029/JC095iC07p11641>
- Martinson, D. G. & Iannuzzi, R. A. (1989). Antarctic ocean-ice interaction: Implications from ocean bulk property distributions in the Weddell Gyre. In M. O. Jeffries (Ed.), *Antarctic sea ice: Physical processes, interactions and variability* (pp. 243–271). Washington, DC: American Geophysical Union (AGU). <https://doi.org/10.1029/AR074p0243>
- Mauritzen, C., & Häkkinen, S. (1997). Influence of sea ice on the thermohaline circulation in the Arctic-North Atlantic Ocean. *Geophysical Research Letters*, 24(24), 3257–3260. <https://doi.org/10.1029/97GL03192>
- Mazloff, M. R., Heimbach, P., & Wunsch, C. (2010). An eddy-permitting Southern Ocean state estimate. *Journal of Physical Oceanography*, 40(5), 880–899. <https://doi.org/10.1175/2009JPO4236.1>
- McGillicuddy, D. J. (2016). Mechanisms of physical-biological-biogeochemical interaction at the oceanic mesoscale. *Annual Review of Marine Science*, 8(1), 125–159. <https://doi.org/10.1146/annurev-marine-010814662-015606>
- McGillicuddy, D. J., Anderson, L. A., Bates, N. R., Bibby, T., Buesseler, K. O., Carlson, C. A., et al. (2007). Eddy/wind interactions stimulate extraordinary mid-ocean plankton blooms. *Science*, 316(5827), 1021–1026. <http://doi.org/10.1126/science.1136256>
- McGillicuddy, D. J., Robinson, A. R., Siegel, D. A., Jannasch, H. W., Johnson, R., Dickey, T. D., et al. (1998). Influence of mesoscale eddies on new production in the Sargasso Sea. *Nature*, 394(6690), 263–266. Retrieved from <http://www.nature.com/articles/10.1038/28367>
- McKee, D. C., Martinson, D. G., & Schofield, O. (2019). Origin and Attenuation of mesoscale structure in circumpolar deep water intrusions to an Antarctic shelf. *Journal of Physical Oceanography*, 49(5), 1293–1318. <https://doi.org/10.1175/JPO-D-18-0133.1>
- McPhee, M. G., Kikuchi, T., Morison, J. H., & Stanton, T. P. (2003). Ocean-to-ice heat flux at the North Pole environmental observatory. *Geophysical Research Letters*, 30(24), 1–5. <https://doi.org/10.1029/2003GL018580>
- McPhee, M. G., Kottmeier, C., & Morison, J. H. (1999). Ocean heat flux in the central Weddell sea during Winter. *Journal of Physical Oceanography*, 29(6), 1166–1179. [https://doi.org/10.1175/1520-0485\(1999\)029<1166:OHFITC>2.0.CO;2](https://doi.org/10.1175/1520-0485(1999)029<1166:OHFITC>2.0.CO;2)
- Moffat, C., & Meredith, M. (2018). Shelf-ocean exchange and hydrography west of the Antarctic peninsula: A reviews. *Philosophical Transactions of the Royal Society A: Mathematical, Physical & Engineering Sciences*, 376(2122), 20170164. <https://doi.org/10.1098/rsta.2017.0164>
- Muench, R. D., Morison, J. H., Padman, L., Martinson, D., Schlosser, P., Huber, B., & Hohmann, R. (2001). Maud rise revisited. *Journal of Geophysical Research: Oceans*, 106(C2), 2423–2440. <https://doi.org/10.1029/2000JC000531>
- Niebauer, H. J., & Smith, W. O., Jr. (1989). A numerical model of mesoscale physical-biological interactions in the Fram Strait marginal ice zone. *Journal of Geophysical Research*, 94(C11), 16151–16175. <https://doi.org/10.1029/JC094iC11p16151>
- Niiler, P. P. (1969). On the Ekman divergence in an oceanic jet. *Journal of Geophysical Research*, 74(28), 7048–7052. <http://doi.wiley.com/10.1029/JC074i028p07048>
- Ohshima, K. I., Nihashi, S., & Iwamoto, K. (2016). Global view of sea-ice production in polynyas and its linkage to dense/bottom water formation. *Geoscience Letters*, 3(1), 13. <https://doi.org/10.1186/s40562-016-0045-4>
- Onarheim, I. H., Smedsrud, L. H., Ingvaldsen, R. B., & Nilsen, F. (2014). Loss of sea ice during winter north of Svalbard. *Tellus A: Dynamic Meteorology and Oceanography*, 66(1), 23933. <https://doi.org/10.3402/tellusa.v66.23933>
- Orsi, A. H., Whitworth, T., & Nowlin, W. D. (1995). On the meridional extent and fronts of the Antarctic Circumpolar Current. *Deep Sea Research Part I: Oceanographic Research Papers*, 42(5), 641–673. [https://doi.org/10.1016/0967-0637\(95\)00021-W](https://doi.org/10.1016/0967-0637(95)00021-W)
- Ou, H. W., & Gordon, A. L. (1986). Spin-down of baroclinic eddies under sea ice. *Journal of Geophysical Research*, 91(C6), 7623. <https://doi.org/10.1029/jc091ic06p07623>
- Padman, L. (1995). Small-scale physical processes in the Arctic ocean. In W. O. Smith Jr. & J. M. Grebmeir (Eds.), *Arctic oceanography: Marginal ice zones and continental shelves* (pp. 97–129). American Geophysical Union (AGU). <https://doi.org/10.1029/CE049p0097>
- Polyakov, I. V., Pnyushkov, A. V., Alkire, M. B., Ashik, I. M., Baumann, T. M., Carmack, E. C., et al. (2017). Greater role for Atlantic inflows on sea-ice loss in the Eurasian basin of the Arctic ocean. *Science*, 356(6335), 285–291. Retrieved from <https://science.sciencemag.org/content/356/6335/285> 10.1126/science.aai8204

- Seo, H. (2017). Distinct influence of Air-sea interactions mediated by mesoscale sea surface temperature and surface current in the Arabian sea. *Journal of Climate*, *30*(20), 8061–8080. <https://doi.org/10.1175/JCLI-D-16-0834.1>
- Sirevaag, A., & Fer, I. (2012). Vertical heat transfer in the Arctic Ocean: The role of double-diffusive mixing. *Journal of Geophysical Research*, *117*(C7), 1–15. <https://doi.org/10.1029/2012JC007910>
- Song, H., Marshall, J., Gaube, P., & McGillicuddy, D. J. (2015). Anomalous chlorofluorocarbon uptake by mesoscale eddies in the Drake Passage region. *Journal of Geophysical Research: Oceans*, *120*(2), 1065–1078. <http://doi.wiley.com/10.1002/2014JC010292>
- Song, H., Marshall, J., McGillicuddy, D. J., Jr., & Seo, H. (2020). Impact of current-wind interaction on vertical processes in the Southern Ocean. *Journal of Geophysical Research: Oceans*, *125*(4), e2020JC016046. <https://doi.org/10.1029/2020JC016046>
- Stern, M. E. (1965). Interaction of a uniform wind stress with a geostrophic vortex. *Deep-Sea Research and Oceanographic Abstracts*, *12*(3), 355–367. [https://doi.org/10.1016/0011-7471\(65\)90007-0](https://doi.org/10.1016/0011-7471(65)90007-0)
- Thomas, L. N., Tandon, A., & Mahadevan, A. (2008). Submesoscale processes and dynamics. In M. W. Hecht & H. Hasumi (Eds.), *Geophysical monograph series* (Vol. 177, pp. 17–38). Washington, DC: American Geophysical Union. <http://doi.wiley.com/10.1029/177GM04>
- Timmermans, M.-L., & Marshall, J. (2020). Understanding Arctic ocean circulation: A review of ocean dynamics in a changing climate. *Journal of Geophysical Research: Oceans*, *125*(4), e2018JC014378. <https://doi.org/10.1029/2018JC014378>
- Timmermans, M.-L., Toole, J., Krishfield, R., & Winsor, P. (2008). Ice-Tethered Profiler observations of the double-diffusive staircase in the Canada Basin thermocline. *Journal of Geophysical Research*, *113*(C1), 1–10. <https://doi.org/10.1029/2008JC004829>
- Toole, J. M., Timmermans, M.-L., Perovich, D. K., Krishfield, R. A., Proshutinsky, A., & Richter-Menge, J. A. (2010). Influences of the ocean surface mixed layer and thermohaline stratification on Arctic Sea ice in the central Canada Basin. *Journal of Geophysical Research*, *115*(C10), 1–14. <https://doi.org/10.1029/2009JC005660>
- Wenegrat, J. O., & Thomas, L. N. (2017). Ekman transport in balanced currents with curvature. *Journal of Physical Oceanography*, *47*(5), 1189–1203. <https://doi.org/10.1175/JPO-D-16-0239.1>
- Williams, R. G., & Follows, M. J. (1998). Eddies make ocean deserts bloom. *Nature*, *394*(6690), 228–229. <https://doi.org/10.1038/28285>
- Wilson, E. A., Riser, S. C., Campbell, E. C., & Wong, A. P. S. (2019). Winter upper-ocean stability and ice-ocean feedbacks in the sea ice-covered Southern Ocean. *Journal of Physical Oceanography*, *49*(4), 1099–1117. <https://doi.org/10.1175/JPO-D-18-0184.1>
- Winton, M. (2000). A reformulated three-layer sea ice model. *Journal of Atmospheric and Oceanic Technology*, *17*(4), 525–531.
- Zhai, X., Johnson, H. L., Marshall, D. P., & Wunsch, C. (2012). On the wind power input to the ocean general circulation. *Journal of Physical Oceanography*, *42*(8), 1357–1365. <https://doi.org/10.1175/JPO-D-12-09.1>
- Zweng, M. M., Reagan, J. R., Antonov, J. I., Locarnini, R. A., Mishonov, A. V., Boyer, T. P., et al. (2013). World ocean atlas 2013. Volume 2, Salinity. NOAA atlas NESDIS 74. National Oceanographic Data Center (U.S.), Ocean Climate Laboratory and United States, Data, and Information Service, National Environmental Satellite. <https://doi.org/10.7289/V5251G4D>